Title: **Intrinsic and Extrinsic Defect-Related Excitons in TMDCs**

Author(s):

Kyrylo Greben*, Sonakshi Arora, Moshe G. Harats, and Kirill I. Bolotin*

Citation:

"Nano Lett. 2020, 20, 4, 2544–2550 ; https://doi.org/10.1021/acs.nanolett.9b05323"

Intrinsic and extrinsic defect-related excitons in TMDCs

Kyrylo Greben[1,], Sonakshi Arora[1,2], Moshe G. Harats[1], and Kirill I. Bolotin[1,*]*

[1] Department of Physics, Freie Universität Berlin, 14195 Berlin, Germany

[2] Department of Quantum Nanoscience, Faculty of Applied Science, Delft University of Technology, 2628 CJ, Delft, The Netherland

*k.greben@fu-berlin.de

*kirill.bolotin@fu-berlin.de

ABSTRACT

We investigate an excitonic peak appearing in low-temperature photoluminescence of monolayer transition metal dichalcogenides (TMDCs), which is commonly associated with defects and disorder. First, to uncover the intrinsic origin of defect-related excitons, we study their dependence on gate voltage, excitation power, and temperature in a prototypical TMDC monolayer, MoS_2. We show that the entire range of behaviors of defect-related excitons can be understood in terms of a simple model, where neutral excitons are bound to ionized donor levels, likely related to sulphur vacancies, with a density of 7×10^{11} cm^{-2}. Second, to study the extrinsic origin of defect-related excitons, we controllably deposit oxygen molecules *in-situ* onto the surface of MoS_2 kept at cryogenic temperature. We find that in addition to trivial p-doping of 3×10^{12} cm^{-2}, oxygen affects the formation of defect-related excitons by functionalizing the vacancy. Combined, our results uncover the origin of defect-related excitons, suggest a simple and conclusive approach to track the functionalization of TMDCs, benchmark device quality, and pave the way towards exciton engineering in hybrid organic-inorganic TMDC devices.

INTRODUCTION

Monolayer Transition Metal Dichalcogenides (TMDCs) are semiconductors with a direct bandgap in the visible range[1,2]. Due to the weak screening and strong electron-hole interactions in these materials, their optical properties are dominated by excitons, bound electron-hole pairs.

To date, the properties of free neutral excitons and exciton complexes such as charged excitons (trions) have been studied and largely understood[3,4]. Binding energies[5–7], formation and dissociation mechanisms[8,9], coherence effects[10], and spin-valley effects[11–17] of these excitons have been identified. In addition to neutral and charged excitonic peaks, a feature that is often attributed to localized, rather than free excitons appears in photoluminescence (PL) spectra of many TMDC devices at low temperatures[18–26]. While it is widely assumed that this feature is related to defects in TMDCs, multiple questions remain unanswered.

First, what is the nature of the defect-related PL feature (D peak)? It has been attributed both to two- and three-particle states as well as to various defect types[18,20,21,27–30]. Second, can the D peak be used as an indicator of a sample quality, i.e. to determine the concentration and type of defects? Third, are defect-related excitons of an extrinsic or intrinsic origin? Previously, the D peak has been ascribed separately to intrinsic structural defects[28,30,31] in TMDCs or to extrinsic impurities on TMDC surface[32–35]. The final and the most interesting question is whether the D peak can be used to gauge chemical functionalization of TMDCs. The field of TMDC functionalization has been quickly developing in recent years thanks to potential applications of functionalized materials as chemical- and bio-sensors[36–39]. Defects are centers of chemical activity in otherwise inert TMDCs, and hence are critical for functionalization[40–45]. At the same time, simple techniques to determine the success and extent of functionalization are lacking[46,47]. Here, we address these questions and elucidate the nature of D excitons.

We study the evolution of the PL spectra of a monolayer MoS_2 in the region of the defect-related peak while tuning multiple experimental variables. In addition to well-studied temperature and laser excitation power dependencies, we analyze the behavior of the D peak with gate voltage and surface functionalization due to oxygen molecules. We then show that all our observations can be understood within a simple mass-action law type model[44,48]. In this model, the defect-related exciton is described as a neutral exciton bound to ionized donor levels close to the edge of the conduction band of MoS_2. These levels are likely related to sulphur vacancies[28,29]. Finally, by controllably depositing oxygen molecules onto MoS_2 *in-situ* at cryogenic temperatures, we show that the D peak additionally has an extrinsic character, i.e. is influenced by the impurities on the surface of MoS_2. We show that this influence is likely caused by oxygen functionalization of sulfur vacancies.

RESULTS

Setup

Our custom setup is designed both for gated low-temperature PL measurements as well as for measurements involving *in-situ* sample annealing and deposition of oxygen molecules. (Fig. 1a). The samples are studied inside an optical cryostat at temperatures ranging from 7 to 300 K. For optical characterization, we use Nikon 50x SLWD objective with NA = 0.5 and the laser excitation wavelength of 532 nm, with power between 0.15 and 30 µW. For gate-dependent PL measurements, we use monolayer MoS_2 field effect transistors (FETs) (Fig. 1b, Inset), fabricated on 300 nm SiO_2/p-Si substrate.

In general, two complications can arise in any experiment attempting controlled deposition of molecules onto a TMDC. First, the surface of an as-prepared TMDC is always covered by a layer of contaminants (e.g. water and organic molecules). Second, deposited molecules may diffuse and merge into clusters on the surface. We developed an approach tackling these difficulties. To remove the layer of contaminants, we microfabricated a Cr/Au (3 nm/70 nm) heater and a thermometer on the same chip in proximity to our sample (Fig.1b). This allows *in-situ* high-temperature annealing (> 400 K) within a few seconds, while the rest of the cryostat is kept at a base temperature (T = 7 K). To avoid problems associated with molecule diffusion and clustering, we added a feed-through nozzle with a 100 µm diameter aperture to our cryostat (Fig. 1a). Oxygen is deposited *in-situ* through this nozzle on top of the sample kept at the base temperature, thus promoting the sticking of oxygen molecules to the surface of MoS_2.

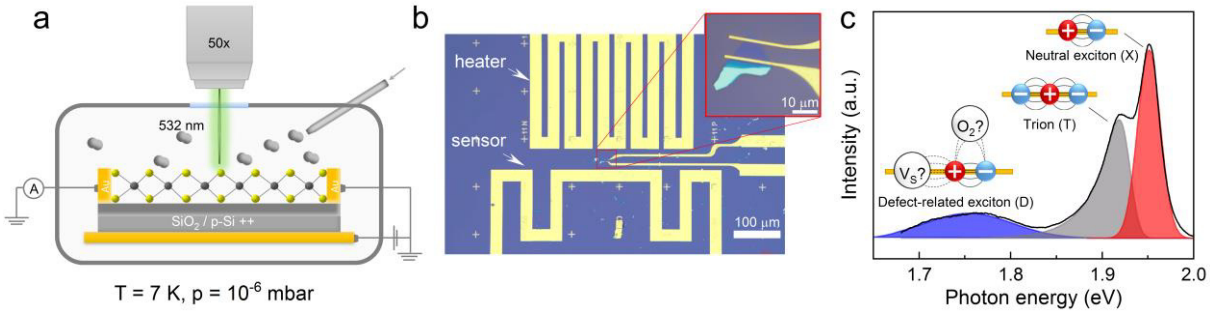

Figure 1: Experimental setup and a typical measurement. (**a**) A cryogenic PL setup customized for in-situ annealing and gas deposition. (**b**) An optical image of the device showing an electrically contacted MoS_2 flake as well as an on-chip resistive thermometer and heater. (**c**) Typical PL spectrum of MoS_2 at cryogenic temperatures showing peaks due to neutral excitons, trions, and defect-related excitons.

Evolution of the low-temperature PL spectra of MoS_2

We study defect-related excitons using low-temperature PL spectroscopy. From the family of TMDCs, we have chosen MoS_2 as a prototypical material with a significant density of intrinsic defects[18,28,29]. A typical PL spectrum of MoS_2 at cryogenic temperatures exhibits three peaks (Fig. 1c). The peak at 1.96 eV, labelled "X", is associated with neutral excitons, while the peak at 1.93 eV, labelled "T" is related to negatively charged excitons (trions). In addition, the peak at 1.77 eV appears in many (but not all) measured samples. This peak, labelled "D", is assumed to relate to disorder[21–23,49–53]. It is the main subject of this work.

In order to elucidate the nature of defect-related excitons in MoS_2, we systematically tune three experimental variables: temperature T, laser excitation power P, and the position of the Fermi level E_F controlled by the backgate voltage V_G (Fig. 2a). We notice that the area under the D peak increases for negative gate voltages, low temperatures, and low illumination powers (Fig. 2b). Conversely, it decreases at high positive gate voltages and completely disappears (at any V_G) for temperatures above 240 K (Fig. 2b). Overall, the D peak changes by over *three* orders of magnitude with V_G and over *four* orders of magnitude with T.

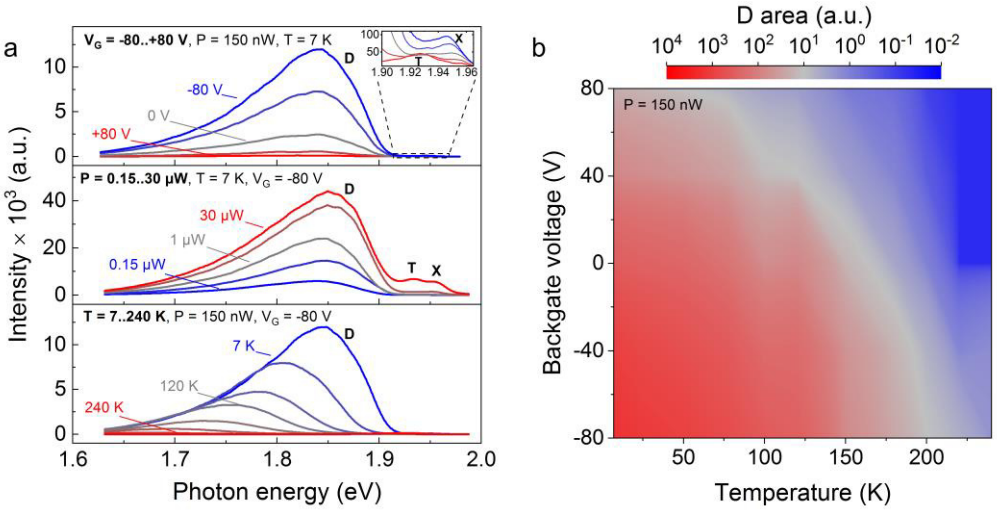

Figure 2: Gate (V_G), temperature (T), excitation power (P) dependence of monolayer MoS_2 photoluminescence. (**a**) PL spectra of monolayer MoS_2 as a function of V_G (top), P (middle) and T (bottom). The inset shows the region of neutral and charged excitons. (**b**) Color map showing V_G and T dependence of the area under the D peak.

Defect-related exciton analysis

Different physical models for defect-related excitons are expected to produce different V_G-, P- and T-dependencies of X, T, and D peaks. We will now show that the dependencies we observe

(Fig. 2) are consistent with a single model: neutral excitons bound to ionized shallow donor levels. Such levels may originate from sulphur vacancies. We start by developing a simple description of our data that is based on mass action law type equations. In this description, the co-existence of neutral excitons (X), trions (T) and free electrons (e) can be viewed as a chemical reaction that has reached its equilibrium, $X + e \leftrightarrow T$ (Supplementary Information and Ref. 48). Similarly, the formation and dissociation of a defect-related exciton (D) from an ionized donor (d), and a neutral exciton can be viewed as a reaction $X + d \leftrightarrow D$. The equality of the rates of forward and reverse reactions leads to the following equations:

$$n_T/n_X = K_T \cdot n_e \qquad (1)$$

$$n_D/n_X = K_D \cdot N_D \qquad (2)$$

Here, n_X, n_T, n_e, are the concentrations of neutral excitons, trions, and of free electrons respectively, while n_D and N_D are concentrations of defect-related excitons and *unoccupied ionized* defect levels. The rate constants $K_T \sim T \cdot exp(-E_T/k_BT)$ and $K_D \sim T \cdot exp(-E_D/k_BT)$ are related to the trion binding energy E_T and the binding energy of the defect-bound exciton E_D. While Eq. 1 was used before to describe exciton/trion equilibrium in TMDCs[44,48], Eq. 2 has not been previously considered, to the best of our knowledge. Both equations can be viewed as a limiting case of a more complex system of equations describing more processes (e.g. creation of free electrons from exciton recombination) in the limit of low excitation powers and long defect exciton lifetime[54].

Equations 1 and 2 provide a simple approach to directly extract the carrier density n_e and the concentration of ionized levels N_D from our experimental data. We fit the spectra in Fig. 2a using Gaussian peaks for defect-bound and neutral excitons. For trions, we use and a more complex fitting function taking into account the electron recoil effect[62] (see Fig. 1c). We then extract the spectral areas under the trion, defect-related, and neutral exciton peaks, A_T, A_D, and A_X, and assume that they are proportional to the respective exciton densities[44]. We extract the experimental dependencies of area ratios A_T/A_X and A_D/A_X on V_G, P, and T from the data in Fig. 2, and plot the resulting analysis in Fig. 3. Finally, from Eqs. 1 and 2 we get $n_e \sim n_T/n_X \sim A_T/A_X$ and $N_D \sim n_D/n_X \sim A_D/A_X$.

We will now show that complex V_G-, P-, and T- dependencies of $n_e \sim A_T/A_X$ and $N_D \sim A_D/A_X$ seen in Fig. 3 have a simple explanation assuming that the density of electrons is controlled by gating and the D peak corresponds to neutral excitons bound to ionized donor levels.

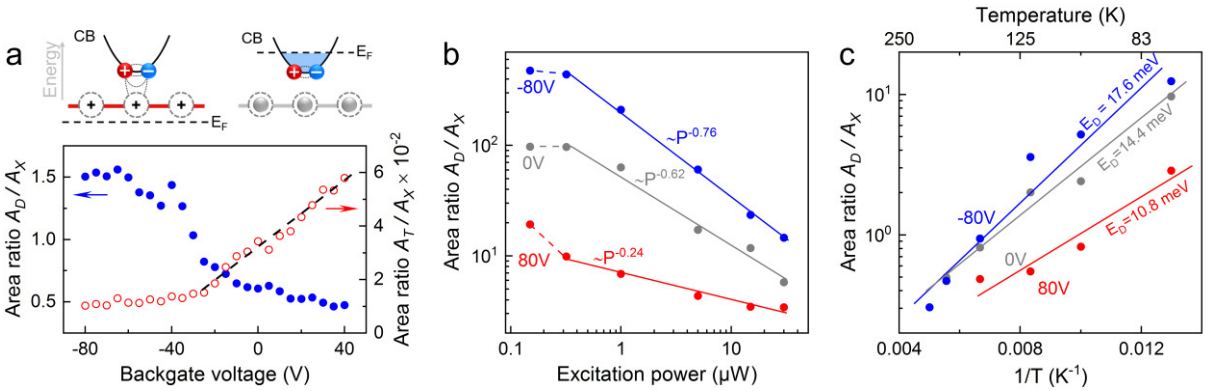

Figure 3: Analysis of defect related excitons. (**a**) V_G-dependence of A_D/A_X, the ratio of areas between defect-related and neutral excitonic peaks (full blue circles, left axis), and A_T/A_X, the ratio of areas between charged and neutral excitonic peaks (open red circles, right axis). The black dashed line is a linear fit. The insets depict the model for defect-bound excitons proposed here: a neutral exciton bound to an ionized donor level. These levels are only ionized when the Fermi level is below these donor levels. (**b**) A_D/A_X vs. excitation power at T = 7 K. Data at different V_G is shown in different colors. Full circles are the experimental points, the solid lines are the power-law fits. (**c**) Arrhenius plot of A_D/A_X for P = 150 nW at different V_G shown in different colors. Full circles are experimental points and the solid lines are linear fits.

The V_G-dependence of both A_T/A_X and A_D/A_X is plotted in Fig. 3a. This data is taken at T = 130 K and P = 1 μW to ensure that the defect-related peak does not dominate the spectrum and that Eq. 1 applies (Fig. 2a and Supplementary Information). We see that A_T/A_X is small and approximately constant below $V_G \approx$ -25 V while increasing roughly linearly with V_G above this value (Fig. 3b, open red circles). This is exactly the behavior expected for n_e: it is zero when E_F is inside the bandgap and $n_e \sim C_G V_G$, where C_G is the gate capacitance, when E_F is above the conduction band minimum (Supplementary Fig. S3). This suggests that the conduction band minima are located at about $V_G \approx$ -25 V (Supplementary Information). At the same time, A_D/A_X increases with decreasing V_G (Fig. 3a, full blue circles). The behavior of A_D/A_X matches the expected V_G-dependence of N_D for a specific defect type: ionized donor level. For large negative V_G, E_F is deep inside the bandgap, and all impurity levels are ionized. In this case, N_D is simply the defect density. In contrast, large positive V_G corresponds to E_F in the conduction band (Fig. 2a, inset). In this case, most of the impurity levels are neutral and hence are unavailable for exciton binding. The rapid increase of A_D/A_X close to the point of E_F crossing into the band edge, $V_G \approx$ -25 V, suggests that the defects are relatively shallow ionized donors. This defect type is consistent with sulphur vacancies which lie 0.3—0.7 eV below the conduction band minimum according to DFT calculations[20,29,52].

Next, we analyze the behavior of A_D/A_X and A_T/A_X with P (Fig. 3b and Supplementary Fig. S1a). A_T/A_X is constant at low powers while growing for $P > 1$ μW. This is also the behavior expected for n_e. At small excitation powers, n_e is equal to the density of background carriers in the sample, while at higher P additional carriers are generated by recombination processes[48]. In contrast, A_D/A_X decreases with P roughly following the power law $A_D/A_X \sim P^a$ with the exponent ranging from $a \sim 0.7$ at V_G = -80 V to $a \sim 0.3$ at V_G = 80 V. In addition, a saturation region is observed at large negative V_G at the smallest $P < 0.5$ μW. This behavior is also consistent with that expected for N_D. For low excitation powers, ionized defect sites become bound by excitons and N_D is close to the defect density. As P increases, there are more excitons generated than the defect sites available, leading to an overall drop in $N_D \sim A_D/A_X$ (see also Supplementary Fig. S5). One can show that under our experimental conditions, the illumination power at which the crossover between the two regimes occurs is related to the defect density (Supplementary Information). From the experimentally-observed crossover at around 0.5 μW, we estimate $N_D = 7 \times 10^{11} cm^{-2}$, close to the density of the sulphur vacancies obtained by other experimental methods[20,30]. Evolution of the saturation point with V_G, evident in Fig. 3b, is also expected in our model, since N_D decreases with increasing V_G (see Fig. 3a). The power law dependence seen in Fig. 3b is consistent with results of calculations[54] and experimental observations[20,26,55].

Finally, we discuss the temperature dependence of A_D/A_X and A_T/A_X (Fig. 3c and Supplementary Fig. 1b). A_T/A_X is weakly temperature-dependent and the trion peak is still visible at room temperature. This is consistent with temperature-independent n_e and large trion binding energy entering into the rate constant K_T[5]. In contrast, A_D/A_Xstrongly decreases with temperature, disappearing for temperatures above 240 K (Fig. 3c). One possible source for the temperature dependence of A_D/A_X is the rate constant K_D in Eq. 2. The activation energy, E_D, entering into it, should relate to the energy difference between neutral and defect-related excitons, ≈ 150 meV. However, a much smaller activation energy, ≈ 17.6 meV at V_G = -80 V, is extracted from Fig. 3c, in agreement with earlier observations[25]. Therefore, we believe that N_D is the dominant source of the T-dependence of A_D/A_X. Sulphur vacancies have been calculated to produce a nearly degenerate doublet with an energy spacing of an order of ≈ 14 meV[51]. We speculate that the redistribution of carriers between these levels contributes to the T-dependence seen in Fig. 3c.

Overall, we see that the dependence of the defect-bound exciton peak on all experimental variables is consistent with that of neutral exciton bound to an ionized donor level likely related

to sulphur vacancies. To the best of our knowledge, no other model for defect-related excitons reported in the literature fits the data of Figs. 2 and 3. First, the carrier density-dependent screening of defect-bound excitons can potentially explain the data similar to Fig. 3a. However, the screening is only effective at carrier densities of order a^{-2}, where a is the real-space exciton size[56,57]. Available estimates put this density at 10^{13} cm^{-2}. In contrast, the largest effect is seen in our data when the Fermi level is inside the bandgap and the density of delocalized electrons is zero. Second, various acceptor levels may be present in MoS_2[25]. However, such defects could not explain the data of Fig. 3a, where the defect peak appears immediately after E_F crosses from the conduction band into the bandgap. Finally, it has been suggested that the defect-related PL peak may result from a two-particle state related to recombination between a free hole and a neutral donor impurity[27]. However, such a state should be favored when E_F is in the conduction band, opposite to what we observe in Fig. 3a.

Extrinsic contribution

Our data so far suggests that the defect-related PL feature stems from neutral excitons bound to an ionized donor level. Such a level may be intrinsic, e.g. originate from a lattice defect in TMDCs such as sulphur vacancies[28,30,31]. However, the defect level may also be extrinsic, and originate from an impurity molecule[32–34]. DFT calculations do suggest that shallow states are affected by adsorbed organic molecules and gases[51,53,58–60]. To further understand the extrinsic *vs.* intrinsic character of the defect level, we controllably deposited a common molecule, oxygen[34,58], onto the surface of MoS_2 kept at cryogenic temperature and examined the evolution of the defect-related peak, D, with time-resolution.

We observe that the PL spectra change dramatically due to annealing and oxygen deposition, especially in the region of the D peak (Fig. 4a). To quantify these changes, we plot A_D/A_X and A_T/A_X at a constant $V_G = 0$ V vs. time with 1 min steps during the deposition process (Fig. 4b). During the first 15 minutes, we observe a drop of A_T/A_X and a rise of A_D/A_X followed by saturation in both quantities. We note that the normalization of A_T and A_D by the neutral exciton area, A_X, accounts for possible changes in PL due to the transparency of deposited layers of molecules. Using the data presented in Fig. 3a,b, we suggest a simple explanation to these trends. Given that our MoS_2 is n-doped, time-dependent behavior of both A_T/A_X and A_D/A_X is consistent with E_F decreasing and moving into the bandgap (Fig. 3a). That, in turn, is indicative of the charge transfer from the TMDC to O_2 molecules. Such charge transfer has been previously seen experimentally[34,61] and predicted computationally[58]. The saturation of charge transfer after 15 minutes suggests that the interaction between the oxygen molecules and a

TMDC becomes negligible after full surface coverage. Two questions remain, however. What is the total density of the transferred charge, and can we explain the spectral changes observed in Fig. 4a simply by a charge transfer model?

To address these questions, we compare the V_G-dependence of the PL spectra before and after O_2 deposition. We pick the spectra of as-exfoliated, annealed, and functionalized states of the sample for which A_T/A_X is the same. We find that the spectra with V_G = -60 V for as-exfoliated, V_G = -40 V for annealed and V_G = 0 V for the spectrum after O_2 deposition have equal A_T/A_X ratios (Fig. 4c). As matching of A_T/A_X indicates equal carrier densities, we conclude that additional carriers produced by the field effect exactly compensate for charge transfer due to the presence of molecules. Therefore, we can calculate the amount of charge transfer in each case using the relation $\Delta n = C_G \Delta V_G$, where $C_G = 7.8 \times 10^{10} V^{-1}\, cm^{-2}$ is the gate capacitance. We obtain a carrier density of $\approx 2.9 \times 10^{12}\, cm^{-2}$ due to saturated O_2 deposition. This is close to the density of the full surface coverage obtained from DFT calculations[34,58]. The removal of adsorbates from the surface of MoS_2 extracts $1.4 \times 10^{12}\, cm^{-2}$ carriers. Therefore, the adsorbates are *n*-dopants.

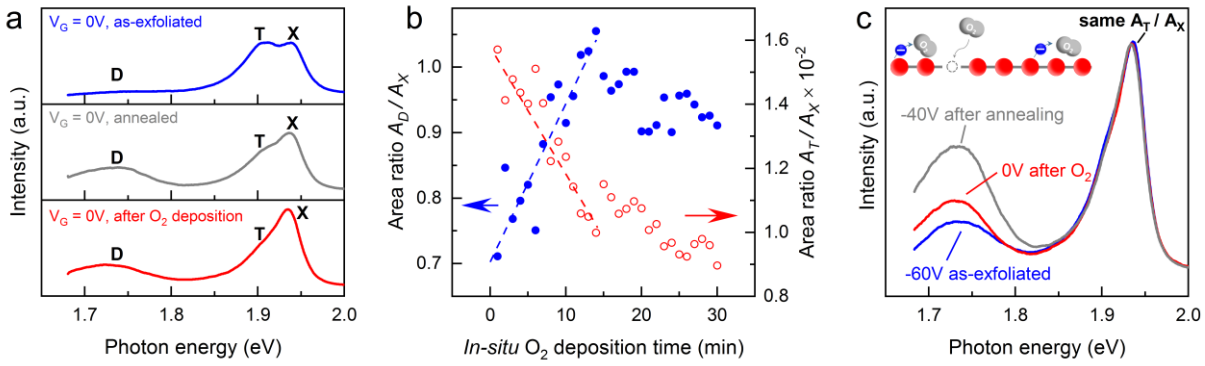

Figure 4: The extrinsic nature of the defect-related excitonic peak. (**a**) PL spectra of MoS_2 at V_G = 0 V at the beginning of measurements (top) after in-situ thermal annealing (middle) and after in-situ O_2 deposition (bottom). (**b**) Changes in A_D/A_X (full blue circles, left axis) and A_T/A_X (open red circles, right axis) with time during in-situ O_2 deposition. (**c**) PL spectra of as-exfoliated at V_G = -60 V, after annealing at V_G = -40 V, and after O_2 deposition at V_G = 0 V. Same A_T/A_X indicates that all three curves correspond to same carrier density in MoS_2.

The most interesting feature of Fig. 4c is that although all curves are matched in the region of the neutral and charged excitons, they starkly differ in the region of the D peak. Specifically, the concentration of unoccupied defect sites $N_D \sim A_D/A_X$ increases after annealing and then drops after O_2 deposition. Therefore, our data cannot be simply explained as a result of charge

transfer. Instead, this observation indicates that the defect-related peak has at least partially extrinsic character. We speculate that defect-related excitons interact with oxygen molecules on the surface of MoS_2 through passivation of a sulfur vacancy by an oxygen molecule, known to eliminate the midgap states accessible for excitons[35]. The increase of N_D after annealing and its subsequent drop after functionalization is consistent with removing and then depositing molecules.

In conclusion, we investigated the dependence of the defect-related feature in the PL spectrum of MoS_2 on multiple experimental variables: temperature, excitation power, gate voltage, and surface coverage. Our data is consistent with a single model for the defect-related exciton: a neutral exciton bound to a shallow ionized donor level close to conduction band minimum. This level likely originates from a sulphur vacancy, but is influenced by oxygen passivation of the defect. To reveal the extrinsic contribution to the defect-related excitons, we developed an approach distinguishing the effects of doping from that of excitons interacting with the defects. Our results have several interesting implications. First, our data allows discriminating between multiple models for the defect-related excitons discussed in the literature. It is inconsistent with the models involving acceptor levels or valence band-midgap state transitions. Second, we show that the presence and the height of the D peak cannot be directly used as an indicator of sample quality, despite the appeal of that simple metric. Instead, a comparison between the samples with the same Fermi level is required. Finally, we prove that molecules on the surface of a TDMC influence midgap states of the TMDC. On one hand, this highlights the necessity of pristine device to study excitonic physics in TMDCs. On the other hand, surface functionalization may open interesting avenues towards controlled defect-engineering of excitonic properties.

ACKNOWLEDGEMENTS

We gratefully acknowledge Denis Yagodkin and Benjamin I. Weintrub for useful discussions and comments. This work was supported by the Deutsche Forschungsgemeinschaft (DFG) - Projektnummer 182087777 - SFB 951 and ERC Starting grant no. 639739.

REFERENCES

1. Splendiani, A. *et al.* Emerging photoluminescence in monolayer MoS2. *Nano Lett.* **10**, 1271–1275 (2010).

2. Mak, K. F., Lee, C., Hone, J., Shan, J. & Heinz, T. F. Atomically thin MoS2: A new direct-gap semiconductor. *Phys. Rev. Lett.* **105**, 136805 (2010).

3. Mueller, T. & Malic, E. Exciton physics and device application of two-dimensional transition metal dichalcogenide semiconductors. *npj 2D Mater. Appl.* **2**, 1–12 (2018).

4. Heine, T. Transition metal chalcogenides: Ultrathin inorganic materials with tunable electronic properties. *Acc. Chem. Res.* **48**, 65–72 (2015).

5. Mak, K. F. *et al.* Tightly bound trions in monolayer MoS2. *Nat. Mater.* **12**, 207–11 (2013).

6. Chernikov, A. *et al.* Exciton binding energy and nonhydrogenic Rydberg series in monolayer WS2. *Phys. Rev. Lett.* **113**, 1–5 (2014).

7. Ugeda, M. M. *et al.* Giant bandgap renormalization and excitonic effects in a monolayer transition metal dichalcogenide semiconductor. *Nat. Mater.* **13**, 1091–1095 (2014).

8. Massicotte, M. *et al.* Dissociation of two-dimensional excitons in monolayer WSe2. *Nat. Commun.* **9**, 1633 (2018).

9. Drüppel, M., Deilmann, T., Krüger, P. & Rohlfing, M. Diversity of trion states and substrate effects in the optical properties of an MoS2 monolayer. *Nat. Commun.* **8**, 2117 (2017).

10. Selig, M. *et al.* Excitonic linewidth and coherence lifetime in monolayer transition metal dichalcogenides. *Nat. Commun.* **7**, 13279 (2016).

11. Xu, X., Yao, W., Xiao, D. & Heinz, T. F. Spin and pseudospins in layered transition metal dichalcogenides. *Nat. Phys.* **10**, 343–350 (2014).

12. Zibouche, N., Philipsen, P., Kuc, A. & Heine, T. Transition-metal dichalcogenide bilayers: Switching materials for spintronic and valleytronic applications. *Phys. Rev. B - Condens. Matter Mater. Phys.* **90**, 1–6 (2014).

13. Li, X. & Moody, G. Valleytronics: Stark control. *Nat. Phys.* **13**, 9–10 (2016).

14. Mak, K. F., He, K., Shan, J. & Heinz, T. F. Control of valley polarization in monolayer MoS2 by optical helicity. *Nat. Nanotechnol.* **7**, 494–498 (2012).

15. Yao, W., Xiao, D. & Niu, Q. Valley-dependent optoelectronics from inversion

symmetry breaking. *Phys. Rev. B - Condens. Matter Mater. Phys.* **77**, 1–7 (2008).

16. Yu, H., Cui, X., Xu, X. & Yao, W. Valley excitons in two-dimensional semiconductors. *Natl. Sci. Rev.* **2**, 57–70 (2015).

17. Onga, M., Zhang, Y., Ideue, T. & Iwasa, Y. Exciton Hall effect in monolayer MoS2. *Nat. Mater.* **216**, 155449 (2017).

18. Hu, Z. *et al.* Two-dimensional transition metal dichalcogenides: interface and defect engineering. *Chem. Soc. Rev.* **47**, 3100–3128 (2018).

19. Zhang, S. *et al.* Defect Structure of Localized Excitons in a WSe2 Monolayer. *Phys. Rev. Lett.* **119**, 1–6 (2017).

20. Tongay, S. *et al.* Defects activated photoluminescence in two-dimensional semiconductors: interplay between bound, charged, and free excitons. *Sci. Rep.* **3**, 2657 (2013).

21. Saigal, N. & Ghosh, S. Evidence for two distinct defect related luminescence features in monolayer MoS2. *Appl. Phys. Lett.* **109**, 122105 (2016).

22. Chow, P. K. *et al.* Defect-Induced Photoluminescence in Monolayer Semiconducting Transition Metal Dichalcogenides. *ACS Nano* **9**, 1520–1527 (2015).

23. Lin, Z. *et al.* Defect engineering of two-dimensional transition metal dichalcogenides. *2D Mater.* **3**, 022002 (2016).

24. Chen, Y. *et al.* Tuning Electronic Structure of Single Layer MoS 2 through Defect and Interface Engineering. *ACS Nano* acsnano.7b08418 (2018). doi:10.1021/acsnano.7b08418

25. Carozo, V. *et al.* Optical identification of sulfur vacancies: Bound excitons at the edges of monolayer tungsten disulfide. *Sci. Adv.* **3**, e1602813 (2017).

26. Wu, Z. & Ni, Z. Spectroscopic investigation of defects in two-dimensional materials. *Nanophotonics* **6**, (2017).

27. Refaely-Abramson, S., Qiu, D. Y., Louie, S. G. & Neaton, J. B. Defect-Induced Modification of Low-Lying Excitons and Valley Selectivity in Monolayer Transition Metal Dichalcogenides. *Phys. Rev. Lett.* **121**, 167402 (2018).

28. Hong, J. *et al.* Exploring atomic defects in molybdenum disulphide monolayers. *Nat.*

Commun. **6**, 6293 (2015).

29. Komsa, H. P. & Krasheninnikov, A. V. Native defects in bulk and monolayer MoS2 from first principles. *Phys. Rev. B - Condens. Matter Mater. Phys.* **91**, 1–17 (2015).

30. Vancso, P. *et al.* The intrinsic defect structure of exfoliated MoS2 single layers revealed by Scanning Tunneling Microscopy. *Sci. Rep.* **6**, 7 (2016).

31. Hong, J., Jin, C., Yuan, J. & Zhang, Z. Atomic Defects in Two-Dimensional Materials: From Single-Atom Spectroscopy to Functionalities in Opto-/Electronics, Nanomagnetism, and Catalysis. *Adv. Mater.* **29**, 1606434 (2017).

32. Ataca, C. & Ciraci, S. Functionalization of Single-Layer MoS 2 Honeycomb Structures. *J. Phys. Chem. C* **115**, 13303–13311 (2011).

33. Lin, Y. C. *et al.* Properties of individual dopant atoms in single-layer MoS2: Atomic structure, migration, and enhanced reactivity. *Adv. Mater.* **26**, 2857–2861 (2014).

34. Tongay, S. *et al.* Broad-Range Modulation of Light Emission in Two-Dimensional Semiconductors by Molecular Physisorption Gating. *Nano Lett.* **13**, 2831–2836 (2013).

35. Barja, S. *et al.* Identifying substitutional oxygen as a prolific point defect in monolayer transition metal dichalcogenides. *Nat. Commun.* **10**, 3382 (2019).

36. Gobbi, M., Orgiu, E. & Samorì, P. When 2D Materials Meet Molecules: Opportunities and Challenges of Hybrid Organic/Inorganic van der Waals Heterostructures. *Adv. Mater.* **30**, 1–20 (2018).

37. Luo, P. *et al.* Doping Engineering and Functionalization of Two Dimensional Metal Chalcogenides. *Nanoscale Horizons* (2018). doi:10.1039/C8NH00150B

38. Hirsch, A. & Hauke, F. Post-Graphene 2D Chemistry: The Emerging Field of Molybdenum Disulfide and Black Phosphorus Functionalization. *Angew. Chemie - Int. Ed.* **57**, 4338–4354 (2018).

39. Huang, Y. L. *et al.* The organic–2D transition metal dichalcogenide heterointerface. *Chem. Soc. Rev.* **47**, 3241–3264 (2018).

40. Ding, Q. *et al.* Basal-Plane Ligand Functionalization on Semiconducting 2H-MoS2Monolayers. *ACS Appl. Mater. Interfaces* **9**, 12734–12742 (2017).

41. Makarova, M., Okawa, Y. & Aono, M. Selective adsorption of thiol molecules at sulfur

vacancies on MoS 2(0001), followed by vacancy repair via S-C dissociation. *J. Phys. Chem. C* **116**, 22411–22416 (2012).

42. Sim, D. M. *et al.* Controlled Doping of Vacancy-Containing Few-Layer MoS2 via Highly Stable Thiol-Based Molecular Chemisorption. *ACS Nano* **9**, 12115–12123 (2015).

43. Cho, K. *et al.* Electrical and Optical Characterization of MoS 2 with Sulfur Vacancy Passivation by Treatment with Alkanethiol Molecules. *ACS Nano* **9**, 8044–8053 (2015).

44. Mouri, S., Miyauchi, Y. & Matsuda, K. Tunable Photoluminescence of Monolayer MoS 2 via Chemical Doping. *Nano Lett.* **13**, 5944–5948 (2013).

45. Chou, S. S. *et al.* Ligand conjugation of chemically exfoliated MoS2. *J. Am. Chem. Soc.* **135**, 4584–4587 (2013).

46. Chen, X., Berner, N. C., Backes, C., Duesberg, G. S. & McDonald, A. R. Functionalization of Two-Dimensional MoS 2 : On the Reaction Between MoS 2 and Organic Thiols. *Angew. Chemie Int. Ed.* **55**, 5803–5808 (2016).

47. Li, Q. *et al.* Towards a Comprehensive Understanding of the Reaction Mechanisms Between Defective MoS2and Thiol Molecules. *Angew. Chemie - Int. Ed.* **56**, 10501–10505 (2017).

48. Ross, J. S. *et al.* Electrical control of neutral and charged excitons in a monolayer semiconductor. *Nat. Commun.* **4**, 1474 (2013).

49. Liu, Y. *et al.* Layer-by-Layer Thinning of MoS 2 by Plasma. *ACS Nano* **7**, 4202–4209 (2013).

50. Ryder, C. R., Wood, J. D., Wells, S. A. & Hersam, M. C. Chemically Tailoring Semiconducting Two-Dimensional Transition Metal Dichalcogenides and Black Phosphorus. *ACS Nano* **10**, 3900–3917 (2016).

51. Qiu, H. *et al.* Hopping transport through defect-induced localized states in molybdenum disulphide. *Nat. Commun.* **4**, 2642 (2013).

52. Zhou, W. *et al.* Intrinsic Structural Defects in Monolayer Molybdenum Disulfide. *Nano Lett.* **13**, 2615–2622 (2013).

53. Komsa, H. P. *et al.* Two-dimensional transition metal dichalcogenides under electron irradiation: Defect production and doping. *Phys. Rev. Lett.* **109**, 1–5 (2012).

54. Schmidt, T., Lischka, K. & Zulehner, W. Excitation-power dependence of the near-band-edge photoluminescence of semiconductors. *Phys. Rev. B* **45**, 8989–8994 (1992).

55. Wu, Z. *et al.* Defects as a factor limiting carrier mobility in WSe2: A spectroscopic investigation. *Nano Res.* **9**, 3622–3631 (2016).

56. Klots, A. R. *et al.* Controlled dynamic screening of excitonic complexes in 2D semiconductors. *Sci. Rep.* **8**, 1–8 (2017).

57. Ando, T., Fowler, A. B. & Stern, F. Electronic properties of two-dimensional systems. *Rev. Mod. Phys.* **54**, 437–672 (1982).

58. Klein, J. *et al.* Robust valley polarization of helium ion modified atomically thin MoS 2. *2D Mater.* **5**, 011007 (2017).

59. Lu, J. *et al.* Atomic healing of defects in transition metal dichalcogenides. *Nano Lett.* **15**, 3524–3532 (2015).

60. Su, W., Jin, L., Qu, X., Huo, D. & Yang, L. Defect passivation induced strong photoluminescence enhancement of rhombic monolayer MoS2. *Phys. Chem. Chem. Phys.* **18**, 14001–14006 (2016).

61. Lee, S. Y. *et al.* Large Work Function Modulation of Monolayer MoS2by Ambient Gases. *ACS Nano* **10**, 6100–6107 (2016).

62. Christopher, J. W., Goldberg, B. B. & Swan, A. K. Long tailed trions in monolayer MoS2: Temperature dependent asymmetry and resulting red-shift of trion photoluminescence spectra. *Sci. Rep.* **7**, 1–8 (2017).

Supplementary information for

Intrinsic and extrinsic defect-related excitons in TMDCs

Kyrylo Greben[1,], Sonakshi Arora[1,2], Moshe G. Harats[1], and Kirill I. Bolotin[1,*]*

[1] Department of Physics, Freie Universität Berlin, 14195 Berlin, Germany

[2] Department of Quantum Nanoscience, Faculty of Applied Science, Delft University of Technology, 2628 CJ, Delft, The Netherland

*k.greben@fu-berlin.de

*kirill.bolotin@fu-berlin.de

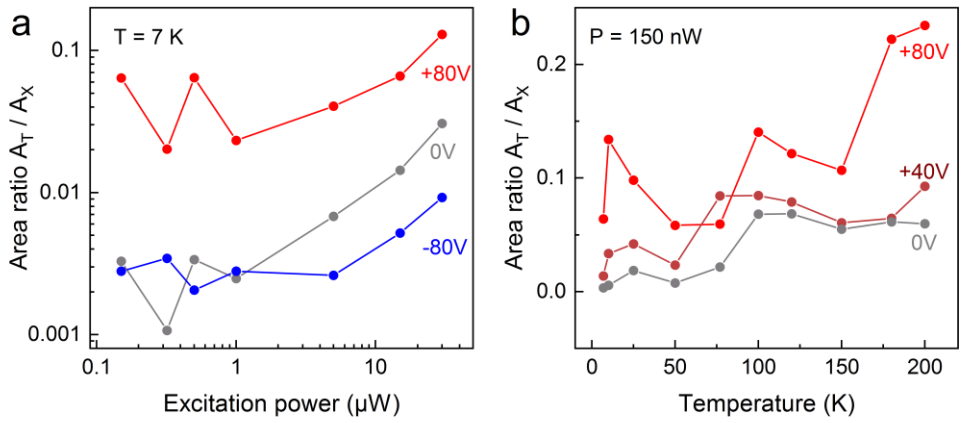

Supplementary Figure S1: Temperature and excitation power dependence of the A_T/A_X ratio. (**a**) The ratio between spectral areas below the trion peak (A_T) and neutral exciton peak (A_X) of monolayer MoS_2 plotted vs. excitation power. Curves for different backgate voltages (V_G) are shown in different colors. A saturation region below 1 μW is visible. (**b**) A_T/A_X vs. temperature, for several different V_G.

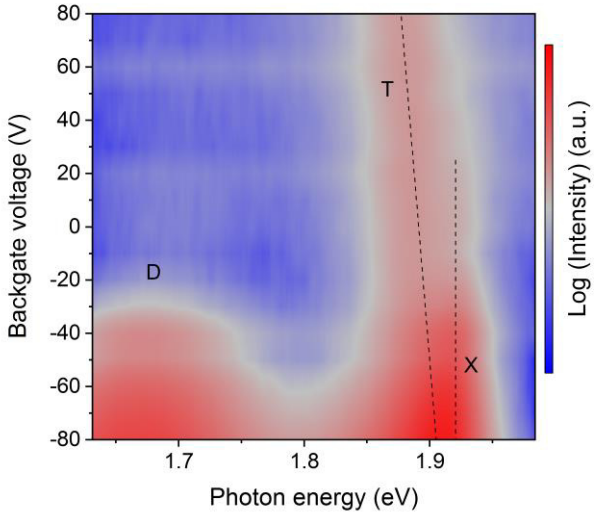

Supplementary Figure S2: Extracting Fermi level position from spectral positions of neutral and charged excitons. PL spectra of monolayer MoS_2 vs. backgate voltage (V_G), plotted as color map. Distinct features corresponding to neutral (X), charged (T) and defect-related (D) excitons are marked. The spectral positions of X and T are denoted with dashed lines. Merging of X and T peaks for $V_G < -40$ is consistent with the E_F reaching the bottom of the conduction band. We use the analysis of Ref. S1 to extract gate dependence of the Fermi level (E_F). Quantitatively, $E^X-E^T=E_F+E_T$, where $E_T \approx 22$ meV is the trion binding energy. The numerical value of the slope $d[E^X(V_G)-E^T(V_G)]/dV_G \sim 0.166$ meV/V corresponds to the effective mass, $m^* = 0.52m_0$, close to numerically calculated effective mass for MoS_2, $0.35m_0$ (Ref.S2).

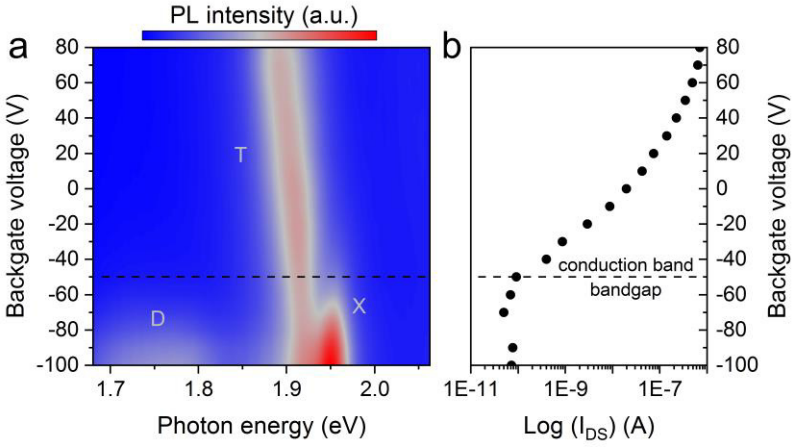

Supplementary Figure S3: Probing defect level position using gate-dependent photoluminescence and electrical transport measurements. (**a**) PL spectra vs. backgate

voltage V_G, plotted as color map for a different sample B. Features related to neutral (X), charged (T) and defect-related (D) excitons emission are marked. The D peak appears only for V_G < -50 V. (**b**) The drain-source current (I_{DS}) vs. V_G for the sample is measured in a field-effect transistor (FET) geometry. At V_G < -50 V the FET switches off. This indicates that E_F reaches the bottom of the conduction band at this voltage. The data of (a) and (b), taken together, suggest that defect-related levels lie inside the bandgap, close to the top of the conduction band.

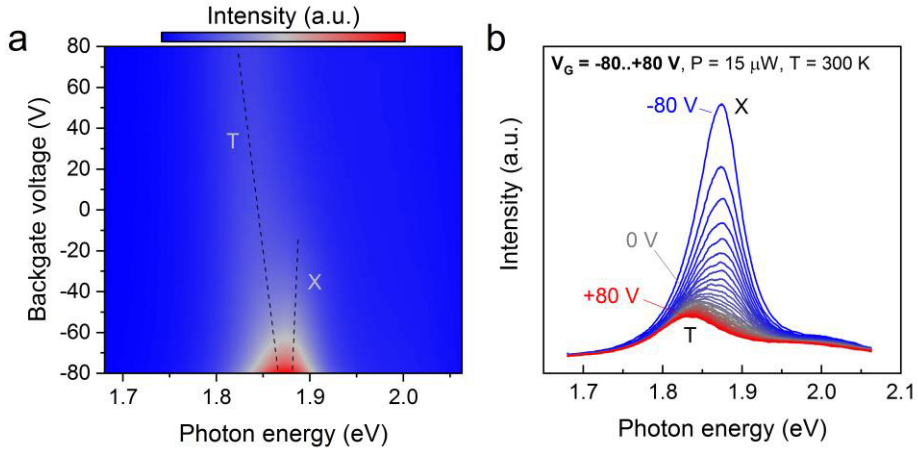

Supplementary Figure S4: Backgate-dependent PL spectra of MoS_2 at room temperature. (**a**) A color map of PL spectra, showing the backgate dependence of neutral (X) and charged (T) exciton features. The dashed lines indicate the spectral positions of X and T. (**b**) Corresponding individual PL spectra. Different colors correspond to different backgate voltages.

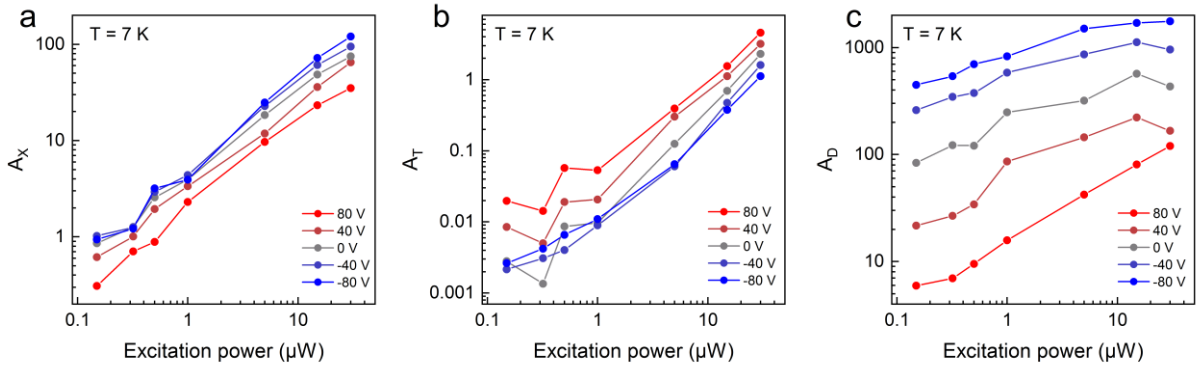

Supplementary Figure S5: The laser excitation power dependence of the spectral areas under neutral (a), charged (b) and defect-related (c) excitons. Different colors indicate different backgate voltages. The data is taken at the temperature of 7 K.

Trion/neutral exciton analysis

The behavior of the neutral exciton and trion can be understood within a simple rate-equation model, as has been first shown in Supplementary Ref. S3. The co-existence of neutral excitons (X), trions (T), and free electrons (e) can be viewed as a chemical reaction that has reached its equilibrium. The equality of the rates of forward and reverse reactions $X + e \leftrightarrow T$ leads to the mass-action law type equation:

$$n_T/n_X = K_T \cdot n_e \quad \text{(S1)}$$

Here n_X, n_T, n_e are the concentrations of neutral excitons, trions, and of free electrons respectively, and $K_T \sim T \cdot exp(-E_T/k_B T)$ is the rate equation constant related to the trion binding energy E_T.

We use Supplementary Eq. S1 to analyze the spectra presented in Fig. 2 of main text. To accomplish this, we obtain the areas and spectral positions of excitonic peaks through fitting (see Main text). We then extract the spectral areas under the trion and neutral exciton peaks, A_T and A_X, and assume that they are proportional to the respective exciton densities[S4]. From Eq. 1 we get $A_T/A_X \sim n_T/n_X \sim n_e$. It is important to note that in general n_e in this equation is the sum of the background electron density, n_b, and the density of photo-excited carriers that is excitation power dependent. However, when the illumination intensity is small enough, $n_e \sim n_b$ (Supplementary Fig. S1a) and the analysis of the Eq. S1 is especially simple.

In the Supplementary Fig. S2 and Fig.3a from the main text, we see that the neutral and defect-related excitons dominate the PL below $V_G \approx$ -25 V, leading to a small and approximately constant A_T/A_X. From the combination of electrical and optical measurements in Supplementary Fig. S3 we know, that trions start to dominate the PL spectrum as soon as the Fermi level (E_F) enters the conduction band. This is due to the V_G-dependent behavior of n_e: it should depend on V_G as $n_e \sim C_G V_G$, where C_G is the gate capacitance when E_F is above the conduction band minima, and $n_e = 0$ when E_F is inside the bandgap. In Supplementary Fig. S2 and Fig. 3a the conduction band minima is located nearly at $V_G \approx$ -25 V. Above this value, A_T/A_X increases roughly linearly with V_G. The position of E_F relative to the conduction band minima is further confirmed from the energy separation between the X and T peaks, indicated with dashed lines in Supplementary Fig. S2. The numerical value of the slope d[$E^X(V_G)$-E^T

(V_G)]/d$V_G \approx 0.166$ meV/V corresponds to the effective mass, m* = 0.52m_0, close to numerically calculated effective mass for MoS_2, 0.35m_0 (Ref.S2).

We also note that A_T/A_X has relatively weak T-dependence (Supplementary Fig. S1b), indicating that trions survive up to room temperature as was previously shown in Supplementary Refs. S3 and S5 and is confirmed in Supplementary Fig. S4. This relatively weak temperature dependence is consistent with the binding energy of the trion, $E_T \sim k_B T \sim 25\ meV$, entering the rate constant, K_T. Finally, both A_T and A_X depend linearly on the excitation power (Supplementary Fig. S5), as expected for free excitons[S6].

Estimating the concentration of defects from saturation measurements

The concentration of defects can be estimated from the experimentally observed saturation in A_D/A_X excitation power dependence (Fig. 3b). Indeed, such saturation is expected when every photoexcited carrier binds to an empty defect level within a lifetime that level (the lifetime of defect-bound exciton). Assuming that all photoexcited excitons eventually bind to defects if they are available, we obtain the following simple estimate for the defect concentration n_d:

$$n_D = \frac{C}{A} \times \frac{P_{sat}}{E_{ph}} \times t \text{ (S1)},$$

Where $C \sim 7\%$ is the absorption coefficient in MoS_2[S5]; $A = \frac{\pi}{4} \times (\frac{1.22\lambda}{NA})^2$ is the area of the laser illumination spot (NA = 0.5 is a numerical aperture of our objective and λ = 532 nm is the excitation wavelength); P_{sat} is the laser excitation power corresponding to the on-set of saturation, and $t \approx 100$ ps is the defect-related exciton lifetime[S7–9]. From this equation we obtain $n_D = 7\times10^{11}$ cm^{-2} for the experimentally observed onset of saturation at P_{sat} = 500 nW.

SUPPLEMENTARY REFERENCES

S1. Chernikov, A. *et al.* Electrical Tuning of Exciton Binding Energies in Monolayer WS2. *Phys. Rev. Lett.* **115**, 1–6 (2015).

S2. Cheiwchanchamnangij, T. & Lambrecht, W. R. L. Quasiparticle band structure calculation of monolayer, bilayer, and bulk MoS2. *Phys. Rev. B* **85**, 205302 (2012).

S3. Ross, J. S. *et al.* Electrical control of neutral and charged excitons in a monolayer

semiconductor. *Nat. Commun.* **4**, 1474 (2013).

S4. Mouri, S., Miyauchi, Y. & Matsuda, K. Tunable Photoluminescence of Monolayer MoS 2 via Chemical Doping. *Nano Lett.* **13**, 5944–5948 (2013).

S5. Mak, K. F. *et al.* Tightly bound trions in monolayer MoS2. *Nat. Mater.* **12**, 207–11 (2013).

S6. Schmidt, T., Lischka, K. & Zulehner, W. Excitation-power dependence of the near-band-edge photoluminescence of semiconductors. *Phys. Rev. B* **45**, 8989–8994 (1992).

S7. Moody, G. *et al.* Microsecond Valley Lifetime of Defect-Bound Excitons in Monolayer WSe2. *Phys. Rev. Lett.* **121**, 57403 (2018).

S8. Robert, C. *et al.* Exciton radiative lifetime in transition metal dichalcogenide monolayers. *Phys. Rev. B - Condens. Matter Mater. Phys.* **93**, 1–10 (2016).

S9. Wang, H. *et al.* Radiative lifetimes of excitons and trions in monolayers of the metal dichalcogenide MoS2. *Phys. Rev. B* **93**, 045407 (2016).